

Interfacial interaction-induced shift of d-band center promotes photocatalytic antibiotics mineralization



Zhangmeng Liu^a, Yue Tian^c, Shuaiqi Yao^b, Yayao Li^b, Yunzhi Fu^{b,*}, Qixin Zhou^{d,*}

^a School of Materials Science and Engineering, Hainan University, Haikou 570228, PR China

^b School of Chemistry and Chemical Engineering, Hainan University, Haikou 570228, PR China

^c School of Marine Science and Engineering, Hainan University, Haikou 570228, PR China

^d Department of Chemistry, Tsinghua University, Beijing 215123, PR China

ARTICLE INFO

Keywords:

N-W bond

IEF, d band shift

Molecular oxygen activation

Photocatalysis mineralization

ABSTRACT

The position and offset of the center of the d band affected by the interface electric field improve the catalytic activity, and the formation of chemical bonds at the interface provides an atomic fast path for electron transfer. In this work, oxygen-containing vacancies in $\text{WO}_{3-x}/\text{C}_3\text{N}_{4+x}$ heterojunction were prepared through the hydrothermal method. UPS and DFT results show that the giant work function difference between WO_{3-x} and C_3N_{4+x} leads to the redistribution of orbital charge at the heterojunction interface, thus creating an interfacial electric field and N-W bond. The upward shift of the center of the W 5d electron orbit triggered the adsorption capacity of $\text{WO}_{3-x}/\text{C}_3\text{N}_{4+x}$ heterojunction for molecular oxygen, which improves photocatalytic degradation efficiency. The degradation of antibiotics in real lake water and the toxicity study by degraded wastewater have demonstrated the thoroughness of mineralization, while the continuous light Fenton system has been shown the stability of the catalyst. This study provides a new insight into the association between the interface electric field and the d-band center, opening a facile avenue for the design of catalysts towards antibiotics photocatalytic mineralization.

1. Introduction

The enhancement of drug resistance for bacteria in water caused by antibiotic pollution has gradually become a thorny problem; this often leads to humans contracting more difficult diseases, increasing the risk of death. Therefore, there is an urgent need for effective tools to prevent and adequately treat drug-resistant infections. Antibiotics and other antimicrobials become ineffective due to drug resistance while requiring an effective strategy to rapidly mineralize antibiotics for reducing bacterial resistance [1–4]. Molecular oxygen activation technology has gradually attracted attention in water environment purification treatment (photocatalysis, electrocatalysis, Fenton reaction) due to its environmentally friendly operation and controllable cost. Efficient molecular oxygen activation is often inseparable from the electronic behavior on the catalyst surface. The activation of oxygen molecules is usually limited by its spin transition, resulting in a very slow activation rate. The goal of molecular oxygen activation can be achieved by controlling the interface behavior of the catalyst to induce excess electron delocalization and directional charge migration [5–7]. However, in past heterogeneous catalysis, the view on the interface effect to regulate

electron behavior to activate molecular oxygen seems less comprehensive [8–13].

The interface electric field can affect the position and offset of the d-band center to improve the catalytic activity. [14–16]. The optimized d-band center can enhance the catalyst's ability to adsorb and activate target substances. Specifically, the difference in the work function makes the orbital electrons of low work function components more easily overflow, causing the electrons on the d orbitals to transfer high work function components near the heterogeneous interface. Electron rearrangement leaves some empty d orbitals that can accept lone pairs of electrons from molecular oxygen. The center of the d band close to the Fermi level is moved up, and the antibonding state of molecular oxygen is promoted to accept the electrons of the d orbitals to activate the $\text{O} \equiv \text{O}$ bond and regulate the spin-forbidden electrons. [17,18].

Research on improving reaction efficiency by focusing on electron transfer between interfacial electric fields has been widely reported. For example, to overcome the problem of low photo-absorption efficiency in photocatalytic global water separation (OWS), Li et al. in situ grown COFs on O-vacancy WO_3 nanowires ($\text{O}_v\text{-}\text{WO}_3$) to construct two-dimensional/two-dimensional Z-scheme heterojunctions with W-O-C

* Corresponding authors.

E-mail addresses: yzhfu@hainanu.edu.cn (Y. Fu), zqx20@mails.tsinghua.edu.cn (Q. Zhou).

chemical bonds, which promoted photocatalytic hydrogen evolution and OWS performance [19]. Wang et al. realized the construction of binary covalent heterostructure by the electrostatic assembly and synthesized ultra-thin CdS-NiFeS 2D-2D heterojunction nanosheets, which enhanced light absorption, promoted charge separation and reduced the reaction barrier [20]. Low et al. reported 2D-2D composites for visible-light-driven CO₂ conversion. Through coupling ultra-thin 2D bismuthine materials with O.V.s modified BMO by electrostatic attraction strategy, 2D-2D Bi/BMOVs nanocomposites with controllable interface charge transfer properties were successfully developed, which significantly improved the charge transfer efficiency for heterojunction photocatalysis system [21]. Yang et al. enlarges the Fermi level gap between WO₃ and C₃N₄ by increasing the concentration of oxygen vacancies in WO₃, enhances the interface electric field in WO₃-C₃N₄-R heterostructures and accelerates the kinetics of ENRR [22]. Li et al. modulated the Z-scheme heterostructure composed of sulfur-rich vacancy ZnIn₂S₄ and MoSe₂ by interfacial Mo-S bond and internal electric field, achieving efficient photocatalytic hydrogen evolution [23]. Although these studies provide a constructive reference for the efficient photocatalytic reaction of atomic interface and internal electric field regulating heterostructure, it is still necessary to deeply study the interface electric field regulating d-band center to improve the catalytic activity in bonded heterojunction.

The in-situ growth method is based on the spontaneous reaction of various metal salt ions in the precursor growth solution under high temperature and high pressure. In this case, the crystalline isomers often have better contact surfaces and possible internal bonding, forming interface electric fields (IEFs) [24]. Furthermore, the design and synthesis of nanoparticles comprising multiple materials linked by solid-state interfaces are essential in photocatalysis. Forming such heterostructures between materials (0D/2D) with different properties can promote the charge separation efficiency on the surface of semiconductor materials and enable broadband absorption by nanometers, thus providing a means to synthesize photocatalysts with desired properties. The photocatalytic degradation process is based on some ideal semiconductor-based nanomaterials [25–27]. In heterogeneous catalysts, the uneven charge distribution caused by the difference in Fermi energy levels of two kinds of semiconductor materials can often enhance the IEF, and the enhancement of IEF can constantly improve the d-band center of the metal elements on the surface of the catalyst [28, 29]. The coordination of metal lattice doped heteroatoms usually changes the electronic structure in the catalyst, thus changing the metal atom's energy level and d orbital [30–33].

In this work, the regulated d-band position of W elements is regulated through N atom coordination, which improved adsorption and activation capabilities for molecular oxygen in the WO_{3-x}/C₃N₄ heterojunction. The effect of IEF on the surface of the catalyst for promoting photocatalytic efficiency is deeply analyzed and discussed, and the molecular oxygen activation mechanism in the photocatalytic reaction is clarified, which provides a new idea for the design of high-performance photocatalysts in energy storage and conversion.

2. Experimental

2.1. Preparation for catalysts

Typically, Na₂WO₄ · 2 H₂O (0.436 g) and PVP (0.0525 g) were dissolved in HCl aqueous solution. Then, well-dispersed carbon nitride aqueous solution was added dropwise under vigorous stirring. After being stirred for six hours, the solution was transferred to a polytetrafluoroethylene lining with a volume of 50 mL and heated at 140 °C for 12 hours. After cooling naturally to room temperature, the product was collected by centrifugation, and the solid product was washed with deionized water and ethanol three times. Finally, the light-yellow powder was dried at 60 °C for 24 h and marked as WO_{3-x}/C₃N_{4+x} heterojunction. Under the same reaction conditions, pure WO₃ was

prepared without introducing carbon nitride. The preparation process of pure carbon nitride was detailed in [supporting information](#) (S.I.).

2.2. Photocatalytic measurement

10 mg of catalyst is ultrasonically dispersed in 50 mL (10 mg·L⁻¹) of tetracycline solution. A 50 mL quartz reaction tank (Jacketed beaker) had a strict condensation system to keep the reaction at a constant temperature (25 °C). All reactions were stirred in the dark for 60 min before illumination to achieve adsorption equilibrium and reduce reaction error. The light source is a 300 W Xenon lamp light source to simulate sunlight. We generally take the mean of three sets of parallel experiments as the test results and use error bars to express them according to the degree of data dispersion; for repeatability experiments, collect the catalysts used in the three sets of parallel experiments, and use deionized water and absolute ethanol to wash three times each, they were placed in a 60°C vacuum drying oven for 24 hours, and the dried samples were collected for repeatability experiments. Photoelectrochemical measurements with theoretical calculation are detailed in SI.

2.3. Characterization

The morphologies of the samples were investigated with the field emission scanning electron microscopy (FE-SEM, Hitachi SU-8010), the transmission electron microscope (TEM, Hitachi HT-7700), the high-resolution transmission electron microscope (HR-TEM, JEOL JEM-2100 F) and the atomic force microscopy (AFM, SPM-9700). X-ray photoelectron spectroscopy (XPS) measurements were performed using an ESCALAB 250Xi instrument (Thermo Scientific) with Al K_α radiation. X-ray diffraction (XRD) patterns of the samples by a Bruker D8 Advance X-ray diffractometer using a Cu K_{α1} ($\lambda=1.5418 \text{ \AA}$) at 45 kV and 200 mA. The Fourier transform infrared (FT-IR) spectra were recorded on Bruker V70 spectrometer. UV-Vis diffuse reflectance spectroscopy (DRS) spectra were acquired through a Hitachi U-3010 spectrophotometer concerning BaSO₄. Interface defects detected single electrons captured using electron paramagnetic resonance (EPR) (Bruker EMXPlus). The monochromatic light resource was a 500 W xenon lamp (CHF XQ500W) with a double-prism monochromator (Omni-λ 3005). The slit width was set at 3 mm. The photovoltage signal was amplified by a lock-in amplifier (SR830-DSP) with a light chopper (SR540). The resolution of the spectrum was 1 nm. The photoluminescence (P.L.) spectra were measured on an Edinburgh FS5 fluorescence spectrometer with an excitation wavelength of 360 nm. All the P.L. tests are performed under dispersion conditions; 1 mg of the sample is uniformly dispersed in 5 mL of deionized water. The entire photocatalytic experiment was conducted using a PLS-SXE300 Xenon lamp light source, with the bulb power controlled at 300 W and simulated sunlight (AM1.5 G, 100 mW cm⁻²) conditions.

2.4. Toxicity assessment of the degradation process

Use *Staphylococcus aureus* as the culture medium to culture mineralized water bodies. Before the experiment, all glass instruments and media solutions were highly sterilized. Suspend *Staphylococcus aureus* in PBS saline solution, then remove the photocatalyst from 2 mL of illuminated T.C. solution, mix it with 100 μL bacterial solution, evenly apply it on an agar plate, and incubate at 37 °C for 12 hours. Finally, the theoretical toxicity of T.C. intermediates was predicted using ECOSAR.

The concentration of pollutants and intermediate products were measured and calculated using an Agilent 1260 high-performance liquid chromatograph (HP-LC) equipped with a 4.6 × 150 mm Eclipse XDB-C185 μm column produced by Agilent. The mobile phase was 80% water and 20% acetonitrile, the sample injection volume was set to 20 μL, the flow rate was 1 mL/min, and the column temperature was 30 °C.

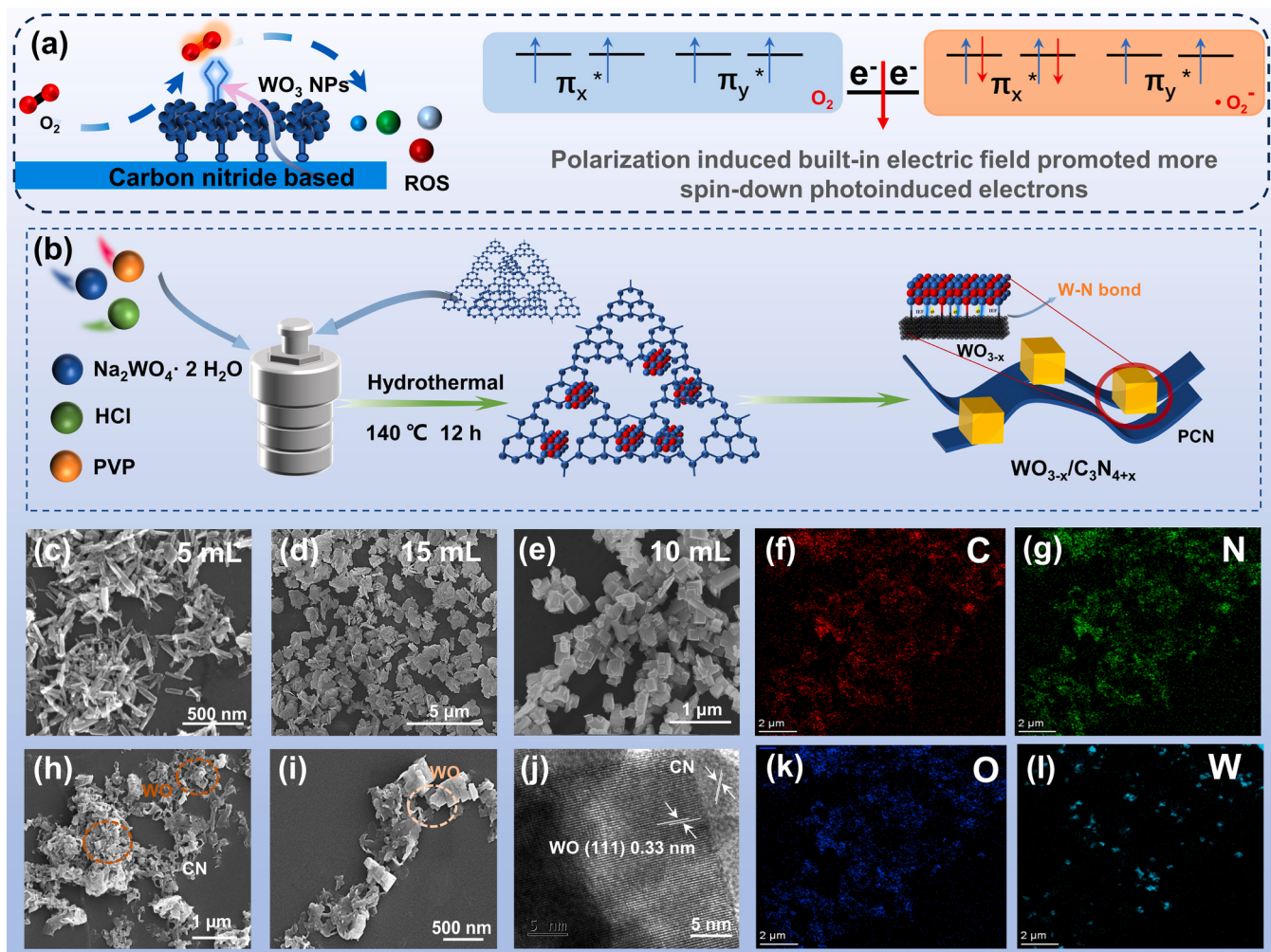


Fig. 1. (a) Schematic description of the reaction pathway for molecular oxygen activation in photocatalyst; (b) Preparation procedure for WO_{3-x}/C_3N_{4+x} heterojunction; (c) - (e) SEM image for WO_3 samples under different conditions; (h) (i) SEM image for WO_{3-x}/C_3N_{4+x} samples; (j) HR-TEM image for heterojunction; (f) - (l) EDX element mapping image of C, N, O, and W in heterojunction.

3. Results and discussion

Specifically, in the process of compounding WO_{3-x} and C_3N_4 , due to the relatively low work function of WO_{3-x} , the electrons in the W 3d orbit are more likely to overflow, causing the d orbital electrons to transfer to the vicinity of C_3N_4 at the heterogeneous interface, resulting in a change in the W 3d orbital configuration and electron rearrangement, leaving some empty d-orbitals that can accept lone pairs from O_2 (molecular oxygen) electrons, and at the same time brings it close to the Fermi level, causing the d band center to move upward, and the antibonding state of molecular oxygen can accept electrons from the d orbital of the W atom, thereby activating the $O\equiv O$ bond, which is to regulate its prohibited spin electrons to promote oxygen activation (Fig. 1(a)). Tungsten oxide (WO_3) with different shapes and exposed crystal planes was prepared by controlling the amount of HCl in the precursor (Fig. 1(b-e)), square tungsten oxide with high exposed crystal plane and oxygen vacancy (WO_{3-x}) is prepared by one-step hydrothermal. When hydrochloric acid was increased from 5 mL to 15 mL, the shape of tungsten oxide changed from a long stick to a cube to a flat shape. The tungsten oxide obtained by hydrothermal treatment of 10 mL HCl was screened through a comparative test of its catalytic activity.

Meanwhile, carbon nitride is introduced into the hydrothermal kettle; it can be found through Spin-trapping spectra of holes for WO_{3-x}/C_3N_{4+x} (Fig. 2(d)) that the heterojunction catalyst obtained by hydrothermal treatment is rich in delocalized electrons, which can prove the

existence of defects and oxygen vacancies. At high temperature and high pressure, H_2WO_4 adsorbed on the surface of carbon nitride fragments dispersed in advance, forming WO_{3-x}/C_3N_{4+x} heterostructures ("3-x" with "4+x" is marking due to the existence of defects and oxygen vacancies) with good contact (Fig. 1(h)). The original C.N. structure prepared does not contain a defect state structure. The defect state only appears after the hydrothermal compounding process with tungsten oxide. This doping state defect may occur because the bulk C.N. structure contains a large amount of incompletely burned urea; during hydrothermal at high temperature, high pressure, and acidic environments, the original C.N. structure is further etched and polymerized. It can be illustrated in the SEM image, XPS, and XRD characterization of the C.N. structure after hydrothermal treatment (Fig. S1).

SEM and TEM observed the surface morphology of the heterostructure. The O-vacancy WO_{3-x} is composed of cube-shaped particles about 50 nm, which are dispersed well on the surface of crimped carbon nitride (Fig. 1(i)). HR-TEM can also observe apparent lattice spacing, and the lattice spacing of 0.331 nm corresponds to the {111} plane of WO_{3-x} (Fig. 1(j)), the irregular short-range disordered lattice with close contact corresponds to the defect carbon nitride. The element distribution mapping fully shows the uniform distribution of C, N, O, and W elements in the heterojunction. In addition, as shown in Fig. S2, in the XRD spectrum of the heterojunction, the diffraction peak of 23.2° , 24.5° , 26.9° , and 34.7° can correspond to WO_{3-x} , compared with the pure phase WO_3 , the diffraction peak shows a slight angle shift, which

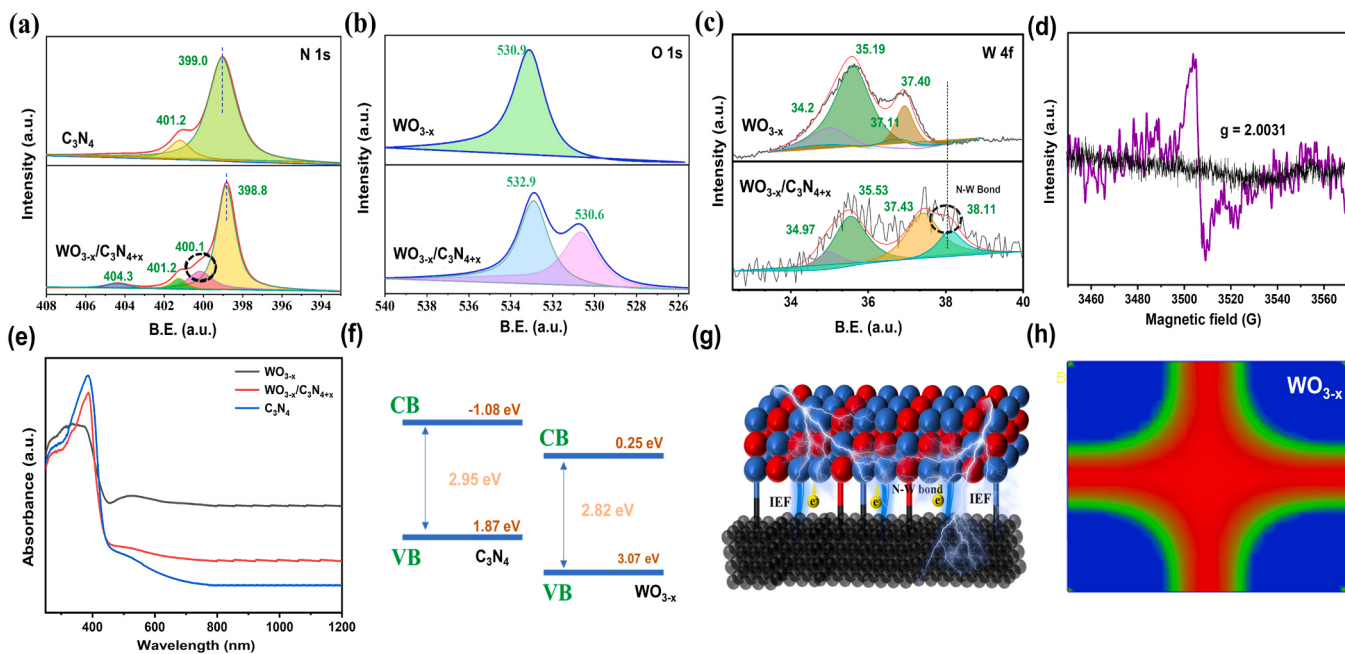


Fig. 2. (a) (b) (c) High-resolution XPS spectra of N 1 s, O 1 s and W 4 f; (d) Spin-trapping spectra of electrons for $\text{WO}_{3-x}/\text{C}_3\text{N}_{4+x}$ in dark and light environments; (e) UV Vis DRS for catalysts; (f) Energy band structure diagram of C_3N_4 and WO_{3-x} ; (g) Schematic diagram of interface N-W bond; (h) Simulated STEM diagram for WO_{3-x} .

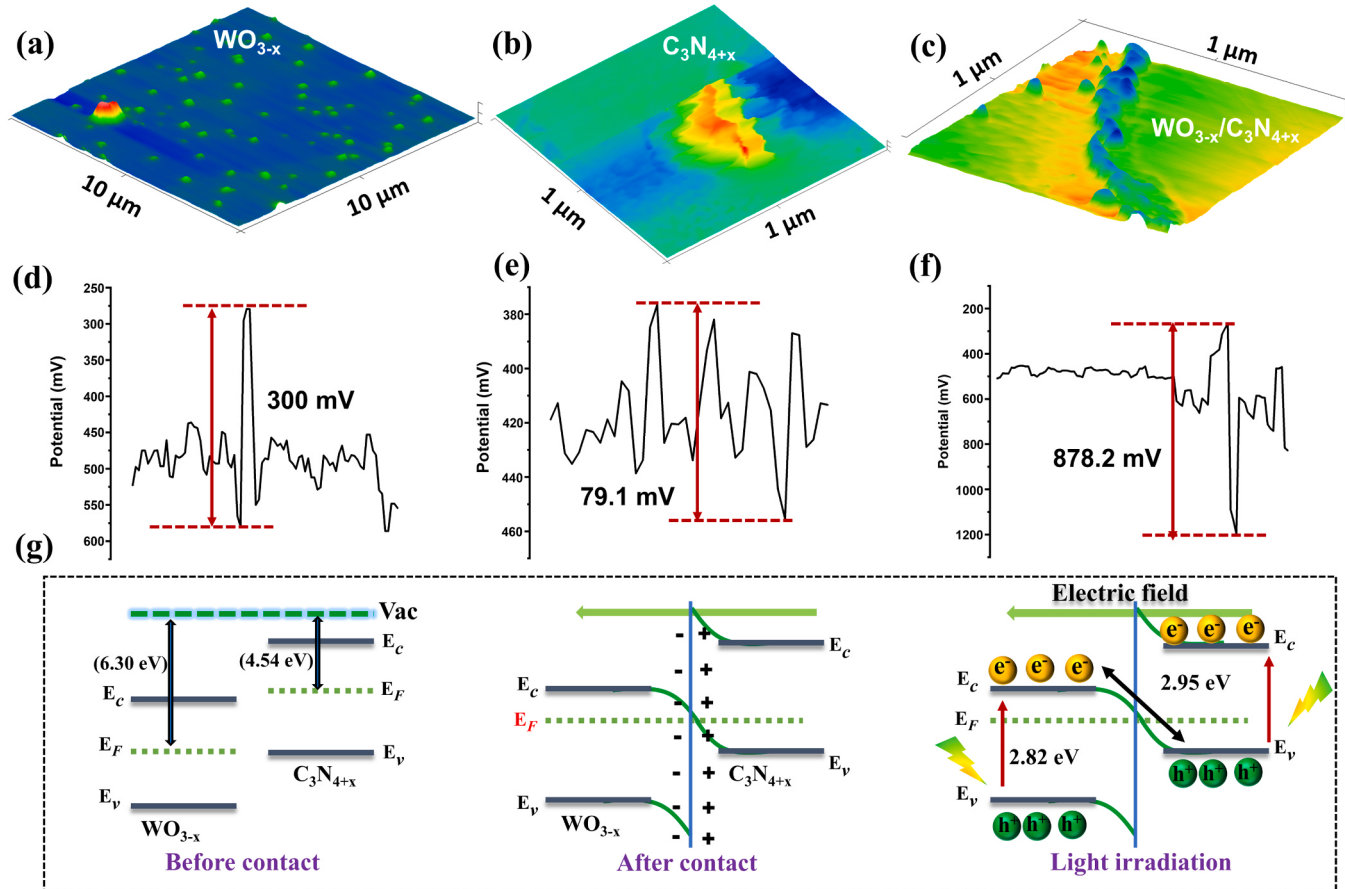


Fig. 3. Surface potential profile of 3D line-scanning for (a)(d) WO_{3-x} , (b)(e) C_3N_4 , (c)(f) $\text{WO}_{3-x}/\text{C}_3\text{N}_{4+x}$ heterojunction; (g) Mechanism diagram of charge flow direction in $\text{WO}_{3-x}/\text{C}_3\text{N}_{4+x}$ heterojunction.

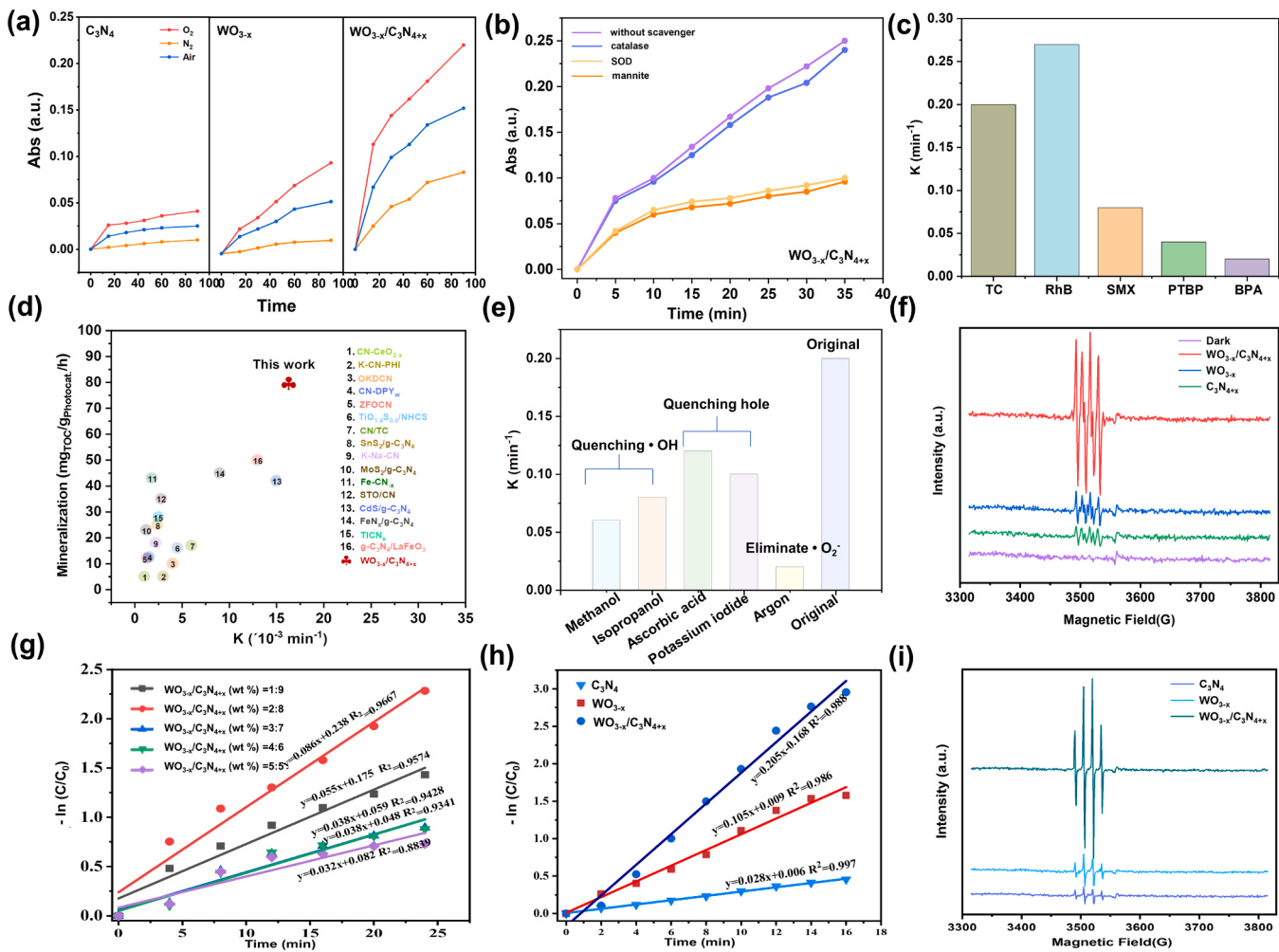


Fig. 4. (a) The absorbance peak monitored for the product at 370 nm vs reaction time under different gas conditions of samples; (b) $\text{WO}_{3-x}/\text{C}_3\text{N}_{4+x}$ in the presence of different scavengers under visible light irradiation; (c) Apparent rate constants for photocatalytic oxidation of five substrates by $\text{WO}_{3-x}/\text{C}_3\text{N}_{4+x}$ under visible light irradiation and the intensity are $\sim 100 \text{ mW cm}^{-2}$; (d) Comparison of K_c and mineralization of TC with those reported in the literature by photocatalysis (References represented by numbers 1–16 are placed in the SI); (e) Influence of quencher and atmosphere on K_c (Photocatalyst: $\text{WO}_{3-x}/\text{C}_3\text{N}_{4+x}$ (5 mg/L); TC (10 mg/L)); (f) Spin-trapping spectra of DMPO- O_2^- in different photo reaction systems; (g) Catalyst degradation first-order kinetic plots for antibiotics under different ratios; (h) Comparison of antibiotics degradation kinetic plots by different catalysts; (i) Spin-trapping spectra of DMPO-OH in different photo reaction systems.

indicates the appearance of oxygen vacancy [34]; the peak corresponding to C_3N_4 appears at 13.6° and 27.3° , and the same slight angle shift indicates that the carbon defect brings the change of triazine ring and π - π stack [35]. The FT-IR spectrum in Fig. S2 shows the stretching vibration peak of W-O-W ($450\text{--}900 \text{ cm}^{-1}$) in WO_{3-x} , the triazine ring stretching vibration peak of carbon nitride (810 cm^{-1}), the C-N and C=N heterocyclic stretching vibration peak ($1250\text{--}1650 \text{ cm}^{-1}$), and the absorption peak of amino group and surface hydroxyl group ($3000\text{--}3500 \text{ cm}^{-1}$). The above results indicate the successful construction of O-vacancy WO_{3-x} and defective carbon nitride heterostructure [36].

Furthermore, the vacancy and defect in $\text{WO}_{3-x}/\text{C}_3\text{N}_{4+x}$ were determined by X-ray photoelectron spectroscopy (XPS). As shown in Fig. 2(b), the O1s peak at $\text{WO}_{3-x}/\text{C}_3\text{N}_{4+x}$ compared with WO_3 (530.6 eV) can be attributed to the lattice defect oxygen species. In the W 4 f spectrum, the peaks at 35.28 eV and 37.28 eV in WO_3 correspond to W^{5+} and W^{6+} , while the peak intensity of W^{5+} in $\text{WO}_{3-x}/\text{C}_3\text{N}_{4+x}$ decreases, indicating that the vacancy is occupied by atoms in C_3N_{4+x} [37]. In addition, the binding energy at 38.11 eV can be attributed to forming the N-W bond. Comparing with N 1 s spectra (Fig. 2(a)), the peaks at 400.1 eV and 404.3 eV in $\text{WO}_{3-x}/\text{C}_3\text{N}_{4+x}$ just proved that the N element in C_3N_{4+x} occupied the oxygen vacancy in WO_{3-x} and formed the interface N-W

bond, which was strongly verified by the shift of the peaks in N 1 s and W 4 f spectra to the opposite direction of binding energy in $\text{WO}_{3-x}/\text{C}_3\text{N}_{4+x}$ [38–40]. The Spin-trapping spectra also prove the existence of many unpaired electrons in the catalyst (Fig. 2(d)), indicating that the presence of the N-W bond promotes the formation of oxygen vacancies and nitrogen defects. The simulated STEM diagram shows that the edge of O-vacancy tungsten oxide with a high exposure plane has more active sites and makes it easier to form bonds (Fig. 2(h)).

To explore the direction of charge flow in $\text{WO}_{3-x}/\text{C}_3\text{N}_{4+x}$ heterojunctions, the samples' work function and energy band structure were obtained through DRS and UPS measurements (Fig. S3). The band gaps of WO_{3-x} and C_3N_4 are calculated as 2.82 eV and 2.95 eV by the Tauc-plot method [41]. Combined with the V.B. values measured by UPS, the conduction band (C.B.) positions of WO_3 and C_3N_4 are 0.25 eV and -1.08 eV , respectively. Fig. 2(e)(f) is a schematic diagram of the heterojunction band structure, in which the negative shift of the CB position indicates the growth shift of the Fermi level, increasing the level gap between the two compounds.

Various measurements were carried out to study the IEF in $\text{WO}_{3-x}/\text{C}_3\text{N}_{4+x}$ heterojunction. Ultraviolet photoelectron spectroscopy (UPS) results show that the work functions of C_3N_4 and WO_{3-x} are 4.55 eV and 3.62 eV, respectively (Fig. S4), indicating that WO_3 is more accessible to

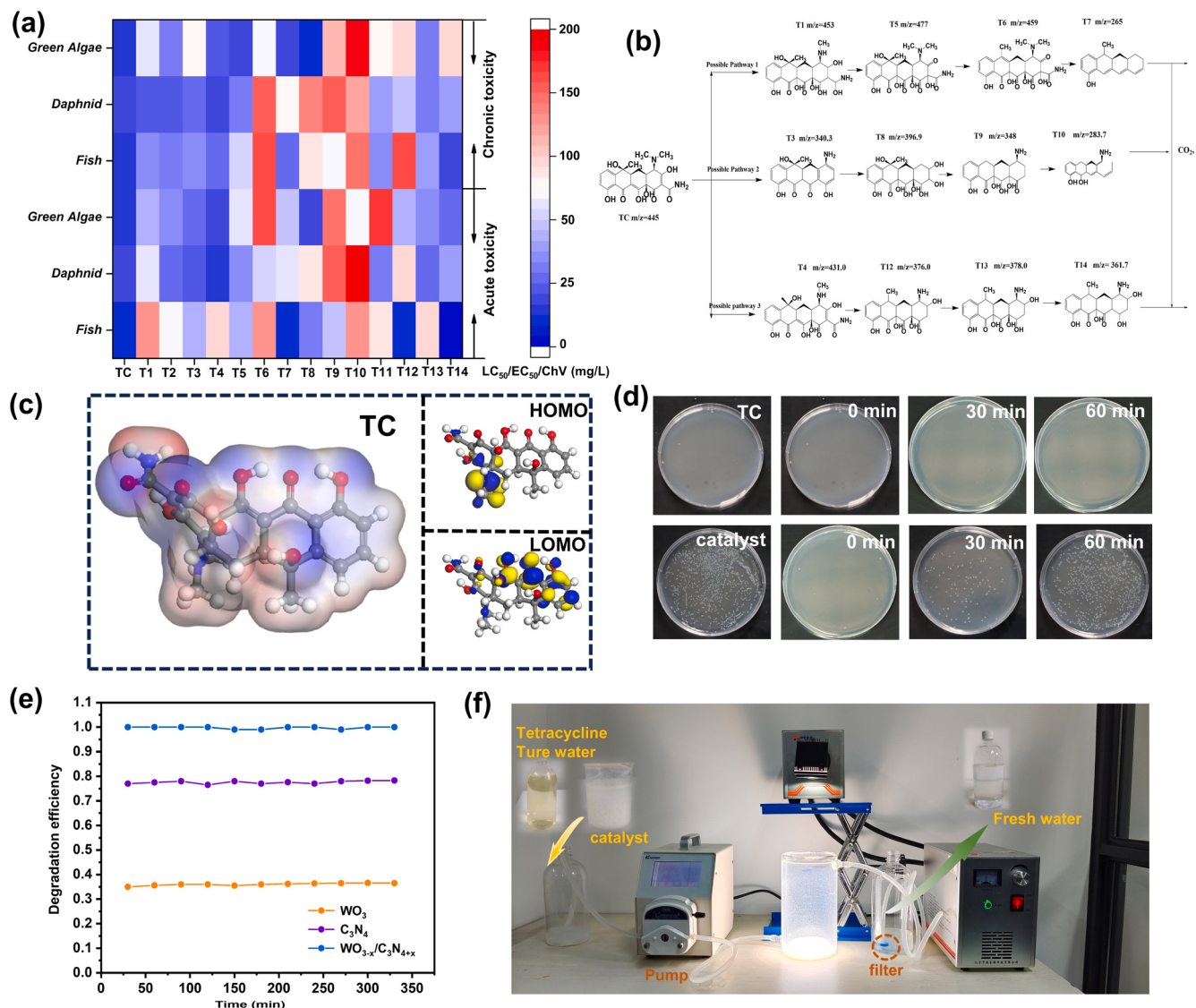


Fig. 5. (a) Predicted acute and chronic toxicity of TC and its degradation intermediates using ECOSAR system; (b) Possible pathways of TC degradation; (c) The electrostatic potential distribution with molecular orbital for TC; (d) Photos of *Staphylococcus aureus* colonies on agar plates; (e) Continuous photo-Fenton reaction for 300 minutes; (f) Picture of the continuous flow photo-Fenton reactor.

release electrons. KPFM is used to measure the surface potential of the catalyst [33,42]. Fig. 3(a)-(f) shows the surface potential distribution of WO_{3-x}, C₃N₄, and WO_{3-x}/C₃N_{4+x}. The corresponding surface potential distribution of the line scan shows that the contact potential difference (CPD) of WO_{3-x}/C₃N_{4+x} (878.2 mV) is much higher than that of WO_{3-x} (300 mV) and C₃N₄ (79.1 mV), indicating the enhancement of interface electric field. The above results show that the N-W bonding between WO_{3-x} and C₃N₄ leads to the formation of strong interface electric field, and the expansion of the Fermi level gap leads to the enhancement of interface electric field in WO_{3-x}/C₃N_{4+x} heterostructures. It is expected that this will be very beneficial in improving the photocatalytic performance of catalysts.

The performance of each catalyst for T.C. degradation was evaluated under AM 1.5 G (100 mW cm⁻²) light. Firstly, the inquiry experiment obtained the WO_{3-x}/C₃N_{4+x} heterojunction with the best mass fraction ratio (wt%). It can be seen that the best ratio of wt% is 2:8 (Fig. S4(a)(b); Fig. 4(g)). All subsequent experiments and characterization take the catalyst obtained under this ratio as the research object. The oxygen activation experiments of the samples were systematically studied. The oxidation rate of TMB under nitrogen, air, and oxygen conditions was tested under simulated sunlight. As shown in Fig. 4(a), the significant

rate difference verified that ROS was formed from O₂. The reaction rate of the sample in oxygen is approximately 3.2 times that in nitrogen. To elucidate the types of ROS during TMB oxidation. Mannitol, superoxide dismutase (SOD), and catalase were introduced into the reaction system (Fig. 4(b)), which could inhibit the generation of •OH, •O₂ and H₂O₂ under visible light irradiation. It clearly shows that SOD can significantly reduce the oxidation of TMB, indicating that •O₂ is the main photogenerated ROS. In addition, the electron spin resonance (ESR) spectrum also further emphasized the intensity of ROS production. As shown in Fig. 4(f)(i), when 5,5-dimethyl-1-pyrroline-N-oxide (DMPO) was added to the reaction system, the spin derivatization signal proved the formation of •O₂. Compared with pure phase WO₃ and CN, WO_{3-x}/C₃N_{4+x} shows a stronger ability to activate O₂ to •O₂. We have also collected some reports on mineralized antibiotics experiments (Fig. 4(d)). It is worth mentioning that less attention has been paid to experiments on the activation of oxygen by catalysts [6,43–47].

The optimum pH value of WO_{3-x}/C₃N_{4+x} for the degradation of T.C. was explored (Fig. S4(c)). When the solution pH = 3.0 was about, the catalyst had the best degradation efficiency and could be completely degraded in 20 min. The weakly acidic solution environment is closer to the actual water environment, and under the optimum pH, the

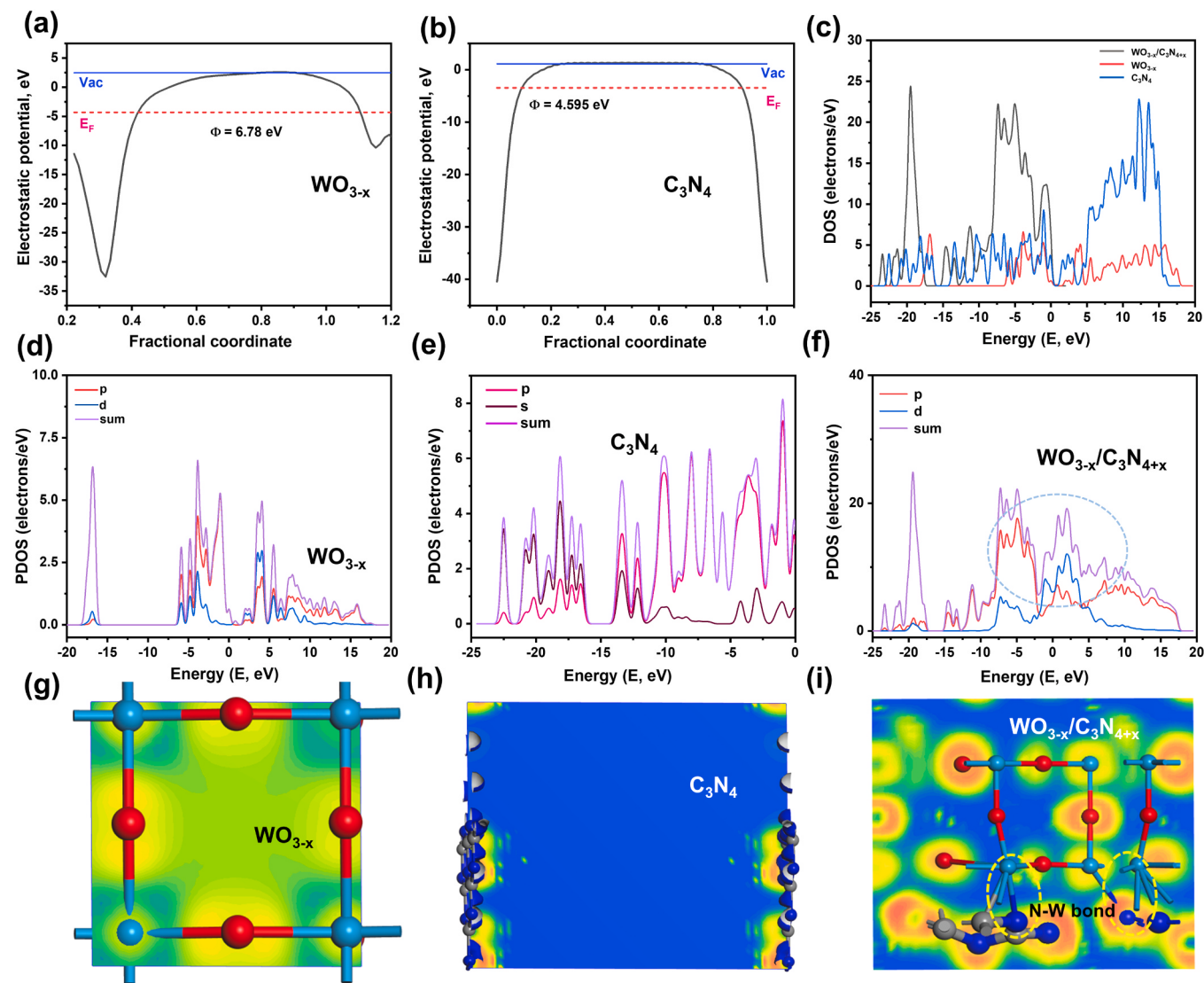


Fig. 6. Difference of electrostatic potential for (a) WO_{3-x} , (b) C_3N_4 , (c) $\text{WO}_{3-x}/\text{C}_3\text{N}_{4+x}$ heterostructure; the energy band structure and corresponding density of states of (d) WO_3 , (e) C_3N_4 , and (f) $\text{WO}_{3-x}/\text{C}_3\text{N}_{4+x}$; (g) (h) The charge density difference for WO_3 and C_3N_4 ; (i) Charge transfer channels in $\text{WO}_{3-x}/\text{C}_3\text{N}_{4+x}$.

degradation efficiency of $\text{WO}_{3-x}/\text{C}_3\text{N}_{4+x}$ is 1.95 times and 7.3 times higher than that of pure WO_{3-x} and C_3N_4 (Fig. 4(h)). Different ionic salts (Na_2CO_3 , NaHCO_3 , NaCl , $\text{Fe}(\text{NO}_3)_3$) are added to the experimental conditions, and Cl^- and NO_3^- have little effect (Fig. S4(f)), indicating that the catalyst can adapt to the water environment with higher salinity. In addition, we added several different antibiotics and organic phenols as target pollutants for degradation experiments. It can be seen that the catalyst has a very good degradation effect on the dye molecule (RhB) and can also degrade more than 80% of SMX within 2 hours. However, the degradation efficiency of two phenolic pollutants (PTBP, BPA) has slightly decreased (Fig. 4(c)). Furthermore, the degradation performance of the catalyst in different natural water bodies was also studied (Fig. S4(g)). It was found that the catalyst's efficiency only decreased slightly in lake water. (Dongpo Lake: Inside Hainan University (Haidian Campus), No. 58 Renmin Avenue, Meilan District, Haikou City. Coordinates: longitude 110.342652, latitude 20.064356.) Still, the subsequent test of mineralization efficiency (Fig. S4(i)) proved that the catalyst had excellent degradation and mineralization efficiency, which was attributed to the superb adsorption and activation efficiency of molecular oxygen in water. The cycle experiment showed that the stability of the catalyst was also outstanding after four cycles (Fig. S4(h)), and the phase structure of the catalyst did not change significantly

(Fig. S5).

Based on the results of HPLC-MS, the possible degradation pathway of TC was predicted, and then the acute and chronic toxicity of TC and its intermediates were evaluated by the ECOSAR program (Fig. 5(a)(b)). It can be seen that a small number of initial intermediates are low toxic to daphnids and algae, and their LC₅₀, EC₅₀, and CHV values are higher, indicating that the toxicity of TC degradation is significantly reduced. Furthermore, bacterial culture was carried out on the mineralized TC solution to explore the thoroughness of the mineralization of antibiotics by the catalyst. As shown in Fig. 5(d), the microflora in the photo-catalytic solution became more evident due to complete mineralization and decreased toxicity, while there were almost no bacteria in the undegraded mineralized solution.

Furthermore, the treatment of actual wastewater by $\text{WO}_{3-x}/\text{C}_3\text{N}_{4+x}$ was studied, and a continuous flow photo Fenton reactor was constructed by using a Xenon lamp light source (Fig. 5(e)(f)). The wastewater containing catalyst was pumped into a continuous flow reactor and exposed to light to initiate a photo-Fenton reaction. Finally, the treated water and catalyst are separated by a membrane filter. We evaluated the degradation of tetracycline by a continuous flow light-Fenton system. Compared with pure WO_{3-x} and C_3N_4 , $\text{WO}_{3-x}/\text{C}_3\text{N}_{4+x}$ shows enhanced degradation performance and removal efficiency,

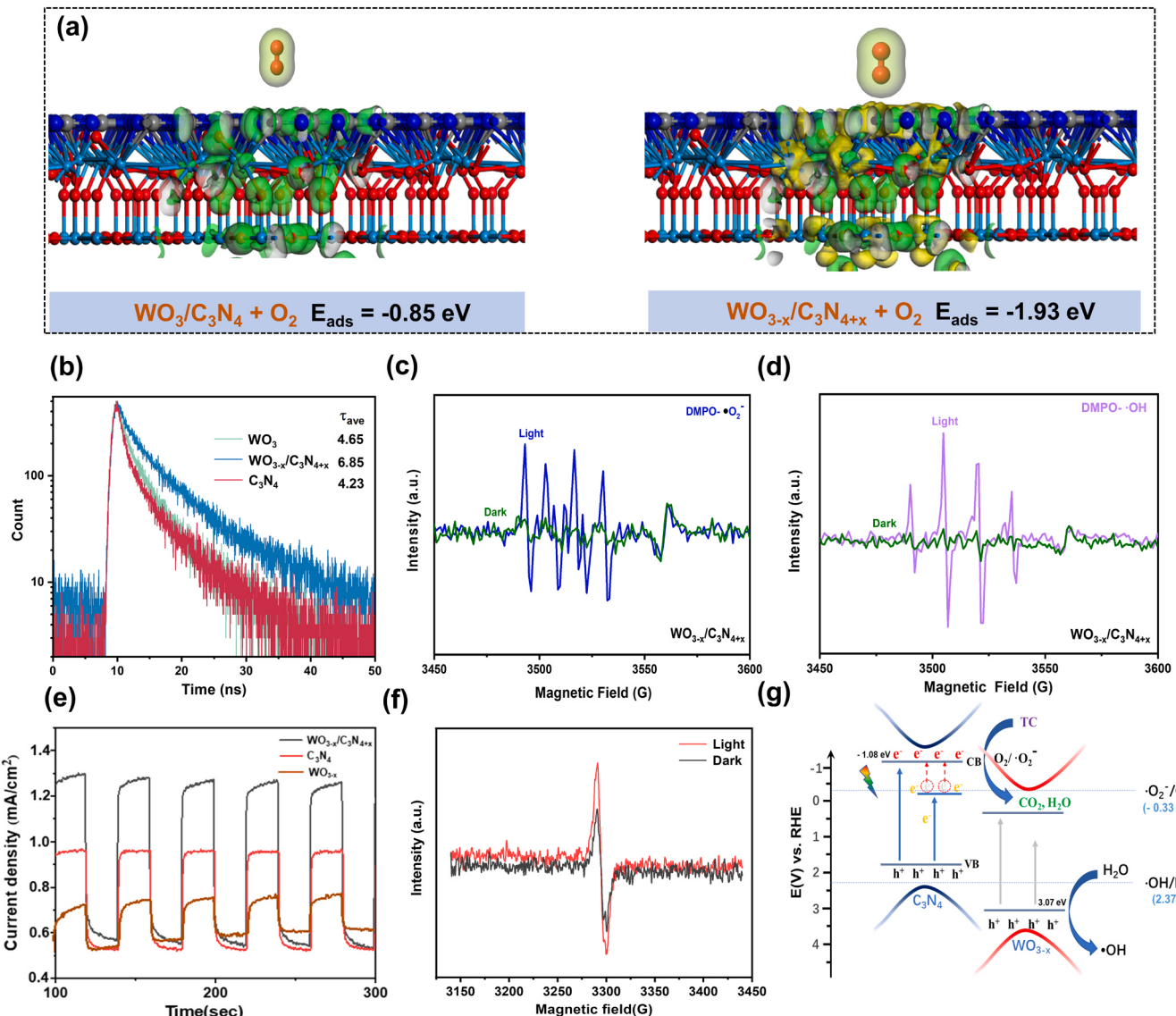


Fig. 7. (a) Calculated charge density difference between $\text{WO}_3/\text{C}_3\text{N}_4$ and $\text{WO}_{3-x}/\text{C}_3\text{N}_{4+x}$ structures; (b) Time-resolved PL decay curves of catalysts monitoring at 440 nm; (c)(d) Spin-trapping spectra of DMPO-OH and (c) DMPO-O₂ for $\text{WO}_{3-x}/\text{C}_3\text{N}_{4+x}$; (e) Difference in photocurrent density between C_3N_4 , WO_{3-x} , and $\text{WO}_{3-x}/\text{C}_3\text{N}_{4+x}$; (f) Spin-trapping spectra of holes for $\text{WO}_{3-x}/\text{C}_3\text{N}_{4+x}$ in dark and light environments; (g) Schematic diagram of the energy band structure of WO_{3-x} and C_3N_4 .

indicating potential practical application value.

The theoretical calculation shows that the d-band center of W elements moves up to the Fermi level, enhancing intermediate species' adsorption in the degradation process. This may be due to the introduction of N element coordination in the W atomic lattice, which changes its electronic structure, resulting in the shift of the center position of the d band, which affects the catalytic activity (Fig. 6 (c)-(f)) [28]. DFT calculates the effect of the interface electric field on the d-band center. The partial density (PDOS) of $\text{WO}_{3-x}/\text{C}_3\text{N}_{4+x}$ shows that the enhancement of the interface electric field can change the d-band center of the W element (Fig. 6(f)) [48]. The interface electric field significantly promotes charge separation, leading to orbital electron rearrangement. Furthermore, to understand the formation mechanism of IEF in $\text{WO}_{3-x}/\text{C}_3\text{N}_{4+x}$ heterojunction in-depth, a series of characterizations of the electron transfer process between WO_{3-x} and C_3N_4 were carried out. First of all, the work functions (W_F) of WO_3 and C_3N_4 are calculated to be 6.78 eV and 4.595 eV, respectively (Fig. 6(a) (b)). The low W_F value of C_3N_4 means its electrons escape from the surface more easily than WO_3 . Secondly, the electronic structure of $\text{WO}_{3-x}/\text{C}_3\text{N}_{4+x}$ is studied by differential charge density analysis and electronic local

function (ELF) [30]. Fig. 6(g)(h)(i) shows the average charge density difference of $\text{WO}_{3-x}/\text{C}_3\text{N}_{4+x}$ in the z-direction, where the red and blue regions are the accumulation and depletion of electrons, respectively. The $\text{WO}_{3-x}/\text{C}_3\text{N}_{4+x}$ heterojunction model shows that the rich charge transfer occurs through the N-W bond, thus forming a solid interface electric field. In addition, compared with the WO_{3-x} region, the C_3N_4 region has a higher electron density (Fig. 6(h)), indicating that electrons have been transferred from WO_{3-x} to C_3N_4 . Fig. 3(g) illustrates the charge transfer process in the $\text{WO}_{3-x}/\text{C}_3\text{N}_{4+x}$ heterojunction and vividly shows the formation of the IEF. Generally speaking, the above results show that the strong IEF is formed due to N-W bonding in $\text{WO}_{3-x}/\text{C}_3\text{N}_{4+x}$ heterojunctions, which enhances the d-band center of W elements, thus enhances the adsorption of intermediates and leads to the improvement of thermo kinetic efficiency of photocatalytic degradation [15].

The calculated CB of WO_3 and CN shows that the photogenerated electrons on the CB of CN can reduce O_2 to $\bullet\text{O}_2^-$ (the standard redox potential of $\text{O}_2/\bullet\text{O}_2^-$ is -0.33 eV vs. NHE). For CN, the corrected VB potential is insufficient to oxidize the adsorbed H_2O to $\cdot\text{OH}$ (the standard redox potential of $\cdot\text{OH}/\text{H}_2\text{O}$ is 2.37 eV). However, WO_3 can be excited to oxidize the adsorbed H_2O to $\cdot\text{OH}$. At the same time, the difference in their

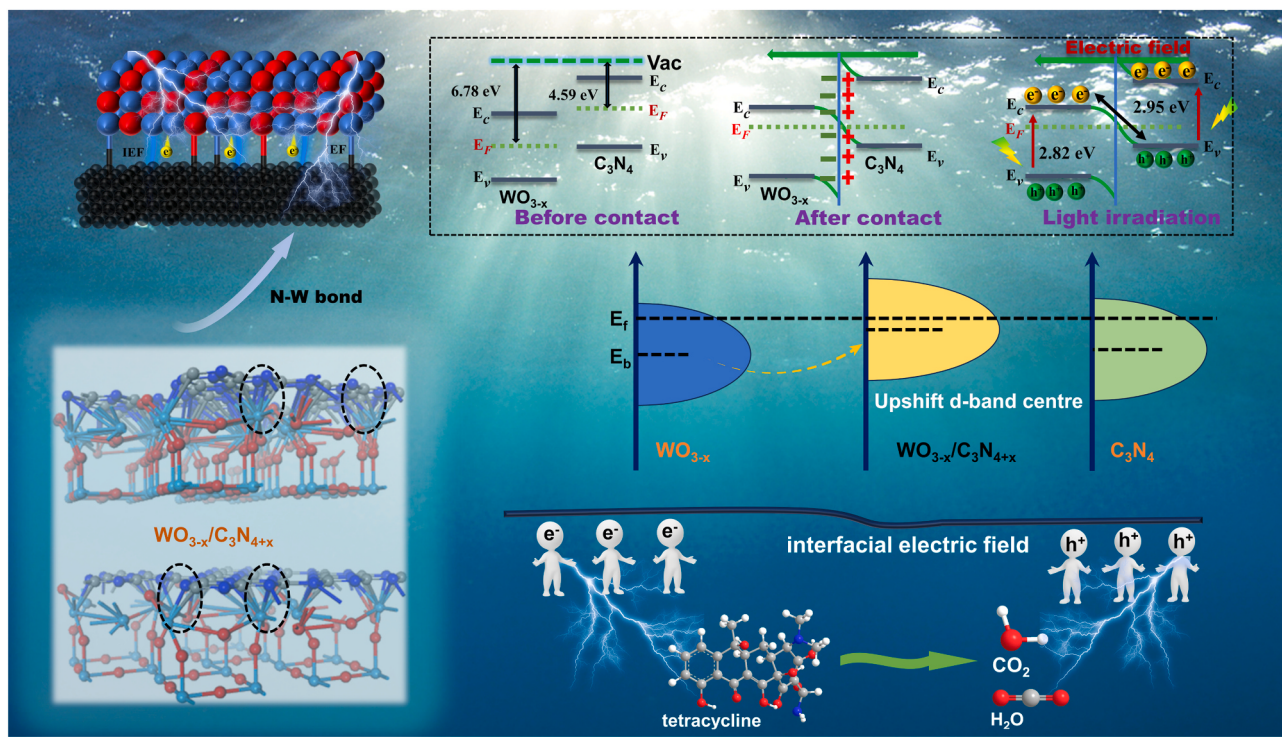


Fig. 8. Schematic illustration of a mechanism for d band shift.

energy bands also leads to a specific direction of electron flow (Fig. 7(g)). This is consistent with the results of the ESR experiment (Fig. 7(c) (d)).

Furthermore, to prove the actual charge separation degree caused by the interface electric field, the fluorescence lifetime and impedance energy Quist diagram of the catalyst were tested. Transient photoluminescence spectra show that $\text{WO}_{3-\text{x}}/\text{C}_3\text{N}_{4+\text{x}}$ shows a longer average carrier lifetime (τ_A) (Fig. 7(b) (e)), and the increase of carrier lifetime τ_A is the crucial factor in enhancing the catalytic activity. The higher photocurrent response and smaller arc radius of $\text{WO}_{3-\text{x}}/\text{C}_3\text{N}_{4+\text{x}}$ indicate that the charge separation degree is the highest (Fig. S6) [49]. Capture experiments show that $\cdot\text{O}_2$ and $\cdot\text{OH}$ are the main active species in the reaction. This is due to the strong redox contributing molecular oxygen activation caused by the band shift (Fig. 4(e)(f)(i)). After conducting degradation experiments using mannitol as $\cdot\text{OH}$ scavenger, we found that $\cdot\text{OH}$ radicals also play a major role in mineralization experiments. We also added methanol and isopropyl alcohol as scavengers for experiments. It can be found that the reaction rate constants are somewhat different, reduced to only $0.06 \sim 0.08 \text{ min}^{-1}$; ascorbic acid and potassium iodide are also used as hole-trapping agents. Compared with the reaction rate of using argon to eliminate reactive oxygen species, the reaction rate can reach 0.125 min^{-1} , slightly lower than that without adding any sacrificial agent, indicating that holes as active groups play a certain role but not the dominant role. The subsequent ESR test showed that compared with pure phase $\text{WO}_{3-\text{x}}$ and C_3N_4 , the change rate of $\cdot\text{OH}$ active groups in $\text{WO}_{3-\text{x}}/\text{C}_3\text{N}_{4+\text{x}}$ was more obvious than that of holes, further confirming the importance of $\cdot\text{OH}$ radicals and the non-dominant role of holes, it may be caused that a large number of holes are consumed by participating in the water oxidation reaction, leaving $\cdot\text{OH}$ to participate in the mineralization reaction (Fig. 7(f)).

As shown in Fig. 8, under the irradiation of simulated sunlight, a large number of photoinduced electrons (e^-) with sufficient energy are transferred from the VB of the C_3N_4 to the CB of the $\text{WO}_{3-\text{x}}$. At the same time, the hole (h^+) remains on the VB of the $\text{WO}_{3-\text{x}}$. It should be pointed out that the abundant O vacancy in $\text{WO}_{3-\text{x}}$ can introduce new donor energy levels into the band gap of $\text{WO}_{3-\text{x}}/\text{C}_3\text{N}_{4+\text{x}}$ and act as an effective

electron trap to inhibit the recombination of photoinduced electron-hole pairs. In addition, driven by the interface chemical bond combined with the built-in electric field, the d-band center of the W atom at the interface shifts upward, and the N-W bond as an atomic interface electron bridge can promote the migration of optically excited carriers between $\text{WO}_{3-\text{x}}$ and C_3N_4 , thus significantly accelerating the charge transfer of Z-scheme. The theoretical calculation results show that the interface-induced electric field effect promotes the asymmetric distribution of charge, which optimizes the adsorption/activation of O_2 intermediates produced in the process of TC degradation (Fig. 7(a)), which is beneficial to the rapid occurrence of TC decomposition and the improvement of degradation efficiency, thus improving the reaction thermo kinetics and enhancing the activity and selectivity of the catalyst.

4. Conclusion

Generally, the interface N-W bond triggered the internal electric field to modulate the d-band center in heterostructures composed of O-vacancy $\text{WO}_{3-\text{x}}$ and defect $\text{C}_3\text{N}_{4+\text{x}}$. Systematic studies show that the charge transfer mechanism induced by the N-W bond and internal electric field regulates the d-band center of W atoms at the interface, and the optimized photocatalyst enhanced molecular oxygen activation to promote simultaneously mineralize and degrade tetracycline hydrochloride in a short time. This work provides valuable inspiration for promoting a photocatalytic performance by consciously regulating Z-scheme charge transfer, and d-band center shift through atomic interface control and internal electric field.

CRediT authorship contribution statement

Yue Tian: Supervision, Project administration, Methodology. **qixin Zhou:** Writing – review & editing, Visualization, Supervision, Project administration. **Zhangmeng Liu:** Writing – original draft, Validation, Data curation, Conceptualization. **Yunzhi Fu:** Project administration, Methodology, Funding acquisition, Formal analysis. **Yayao Li:** Resources, Investigation. **shuaiqi Yao:** Validation, Software.

Declaration of Competing Interest

The authors declare that they have no known competing financial interests or personal relationships that could have appeared to influence the work reported in this paper.

Data Availability

Data will be made available on request.

Acknowledgements

This work was financially supported by the National Natural Science Foundation of China (No. 22162009).

Appendix A. Supporting information

Supplementary data associated with this article can be found in the online version at doi:10.1016/j.apcatb.2024.123998.

References

- [1] W. Shi, Y. Liu, W. Sun, Y. Hong, X. Li, X. Lin, F. Guo, J. Shi, Improvement of synergistic effect photocatalytic/peroxymonosulfate activation for degradation of amoxicillin using carbon dots anchored on rod-like CoFe₂O₄, Chin. J. Chem. Eng. 52 (2022) 136–145.
- [2] J. Zhou, X. Yang, Q. Wei, Y. Lan, J. Guo, Co₃O₄ anchored on biochar derived from chitosan (Co₃O₄@BCC) as a catalyst to efficiently activate peroxymonosulfate (PMS) for degradation of phenacetin, J. Environ. Manag. 327 (2023) 116895.
- [3] Y. Zhang, Y. Li, H. Bi, S. Zhou, J. Chen, S. Zhang, Y. Huang, F. Chang, H. Zhang, T. Wågberg, Nanomanganese cobaltate-decorated halloysite nanotubes for the complete degradation of ornidazole via peroxymonosulfate activation, J. Colloid Interface Sci. 630 (2023) 855–866.
- [4] H. Li, H. Ji, J. Liu, W. Liu, F. Li, Z. Shen, Interfacial modulation of ZnIn₂S₄ with high active Zr-S₄ sites for boosting photocatalytic activation of oxygen and degradation of emerging contaminant, Appl. Catal. B Environ. 328 (2023) 122481.
- [5] M. Xu, Y. Chen, J. Qin, Y. Feng, W. Li, W. Chen, J. Zhu, H. Li, Z. Bian, Unveiling the role of defects on oxygen activation and photodegradation of organic pollutants, Environ. Sci. Technol. 52 (2018) 13879–13886.
- [6] X. Wang, J. Xie, S. Li, Z. Yuan, Y. Sun, X. Gao, Z. Tang, H. Zhang, J. Li, S. Wang, Z. Yang, Y.-M. Yan, Enhancing interfacial electric field in WO₃-C₃N₄ through fermi level modulation for electrocatalytic nitrogen reduction, Appl. Catal. B Environ. 339 (2023) 123126.
- [7] K. Gao, M. Zhou, Y. Liu, S. Wang, R. Fu, Z. Wang, J. Guo, Z. Liu, H. Wang, Y. Zhao, Q. Wang, The dual built-in electric fields across CoS/MoS₂ heterojunctions for energy-saving hydrogen production coupled with sulfion degradation, J. Colloid Interface Sci. 657 (2024) 290–299.
- [8] R. Guo, B. Xi, C. Guo, N. Lv, J. Xu, Comprehensive insight into heterogeneous persulfate activation for environmental pollutants degradation: approaches and mechanism, Environ. Funct. Mater. (2022).
- [9] H. Zhang, C. Xie, L. Chen, J. Duan, F. Li, W. Liu, Different reaction mechanisms of SO₄²⁻ and •OH with organic compound interpreted at molecular orbital level in Co (II)/peroxymonosulfate catalytic activation system, Water Res. 229 (2023) 119392.
- [10] L. Wu, S. Zuo, Y. Zhu, Q. Wang, D. Li, Coordination-driven boron and copper on carbon nitride for peroxymonosulfate activation to efficiently degrade organic contaminants, Sep. Purif. Technol. 312 (2023) 123349.
- [11] H. Anwer, A. Mahmood, J. Lee, K.-H. Kim, J.-W. Park, A.C.K. Yip, Photocatalysts for degradation of dyes in industrial effluents: opportunities and challenges, Nano Res. 12 (2019) 955–972.
- [12] O. Baaloudj, I. Assadi, N. Nasrallah, A. El Jery, L. Khezami, A.A. Assadi, Simultaneous removal of antibiotics and inactivation of antibiotic-resistant bacteria by photocatalysis: a review, J. Water Process Eng. 42 (2021) 102089.
- [13] Z. Cai, L. Huang, X. Quan, Z. Zhao, Y. Shi, G. Li Puma, Acetate production from inorganic carbon (HCO₃⁻) in photo-assisted biocathode microbial electrosynthesis systems using WO₃/MoO₃/g-C₃N₄ heterojunctions and *Serratia marcescens* species, Appl. Catal. B: Environ. 267 (2020) 118611.
- [14] X. Wang, S. Li, Z. Yuan, Y. Sun, Z. Tang, X. Gao, H. Zhang, J. Li, S. Wang, D. Yang, Optimizing electrocatalytic nitrogen reduction via interfacial electric field modulation: elevating d-Band Center in WS₂-WO₃ for enhanced intermediate adsorption, Angew. Chem. 135 (2023) e202303794.
- [15] H. Choi, S. Surendran, Y. Sim, M. Je, G. Janani, H. Choi, J.K. Kim, U. Sim, Enhanced electrocatalytic full water-splitting reaction by interfacial electric field in 2D/2D heterojunction, Chem. Eng. J. 450 (2022) 137789.
- [16] H. Wu, W. Yan, Y. Xing, L. Li, J. Liu, L. Li, P. Huang, C. Lai, C. Wang, W. Chen, Tailoring the interfacial electric field using silicon nanoparticles for stable zinc-ion batteries, Adv. Funct. Mater. (2023) 2213882.
- [17] Y. Wang, M. Liu, F. Fan, G. Li, J. Duan, Y. Li, G. Jiang, W. Yao, Enhanced full-spectrum photocatalytic activity of 3D carbon-coated C₃N₄ nanowires via giant interfacial electric field, Appl. Catal. B: Environ. 318 (2022) 121829.
- [18] J. Jing, J. Yang, W. Li, Z. Wu, Y. Zhu, Construction of interfacial electric field via dual-porphyrin heterostructure boosting photocatalytic hydrogen evolution, Adv. Mater. 34 (2022) 2106807.
- [19] R. Shen, G. Liang, L. Hao, P. Zhang, X. Li, In-situ synthesis of chemically bonded 2D/2D Covalent Organic Frameworks/O-vacancy WO₃ Z-scheme heterostructure for photocatalytic overall water splitting, Adv. Mater. (2023) 2303649.
- [20] G. Sun, Z. Tai, F. Li, Q. Ye, T. Wang, Z. Fang, X. Hou, L. Jia, H. Wang, Noble-metal-free ultrathin CdS-NiFeS 2D–2D heterojunction nanosheets for significantly enhanced photocatalytic hydrogen evolution, ACS Sustain. Chem. Eng. 11 (2023) 4009–4019.
- [21] J. Wang, P. Li, Y. Wang, Z. Liu, D. Wang, J. Liang, Q. Fan, New strategy for the persistent photocatalytic reduction of U(VI): utilization and storage of solar energy in K(+) and Cyano Co-Decorated Poly(Heptazine Imide), Adv. Sci. (Weinh.) 10 (2023) e2205542.
- [22] X. Wang, J. Xie, S. Li, Z. Yuan, Y. Sun, X. Gao, Z. Tang, H. Zhang, J. Li, S. Wang, Enhancing interfacial electric field in WO₃-C₃N₄ through fermi level modulation for electrocatalytic nitrogen reduction, Appl. Catal. B Environ. (2023) 123126.
- [23] S. Li, X. Yang, Z. Cui, Y. Xu, Z. Niu, P. Li, D. Pan, W. Wu, Efficient photoreduction strategy for uranium immobilization based on graphite carbon nitride/perovskite oxide heterojunction nanocomposites, Appl. Catal. B Environ. 298 (2021).
- [24] S. Sharma, G. Sharma, A. Kumar, P. Dhiman, T.S. AlGarni, M. Naushad, Z. A. Alothman, F.J. Stadler, Controlled synthesis of porous Zn/Fe based layered double hydroxides: synthesis mechanism, and ciprofloxacin adsorption, Sep. Purif. Technol. 278 (2021) 119481.
- [25] Y. Shi, Z. Yang, L. Shi, H. Li, X. Liu, X. Zhang, J. Cheng, C. Liang, S. Cao, F. Guo, X. Liu, Z. Ai, L. Zhang, Surface boronizing can weaken the excitonic effects of BiOBr nanosheets for efficient O₂ activation and selective NO oxidation under visible light irradiation, Environ. Sci. Technol. 56 (2022) 14478–14486.
- [26] X. Shen, W. Liu, X. Gao, Z. Lu, X. Wu, X. Gao, Mechanisms of oxidase and superoxide dismutase-like activities of gold, silver, platinum, and palladium, and their alloys: a general way to the activation of molecular oxygen, J. Am. Chem. Soc. 137 (2015) 15882–15891.
- [27] L. Pan, M. Ai, C. Huang, L. Yin, X. Liu, R. Zhang, S. Wang, Z. Jiang, X. Zhang, J. J. Zou, W. Mi, Manipulating spin polarization of titanium dioxide for efficient photocatalysis, Nat. Commun. 11 (2020) 418.
- [28] J. Wang, Y. Zhang, S. Jiang, C. Sun, S. Song, Regulation of d-band centers in localized CdS homojunctions through facet control for improved photocatalytic water splitting, Angew. Chem. (2023) e202307808.
- [29] L. Wang, W.-W. Tian, W. Zhang, F. Yu, Z.-Y. Yuan, Boosting oxygen electrocatalytic performance of Cu atom by engineering the d-band center via secondary heteroatomic phosphorus modulation, Appl. Catal. B Environ. 338 (2023) 123043.
- [30] J. Yin, J. Jin, Z. Yin, L. Zhu, X. Du, Y. Peng, P. Xi, C.-H. Yan, S. Sun, The built-in electric field across FeN/Fe₃N interface for efficient electrochemical reduction of CO₂ to CO, Nat. Commun. 14 (2023) 1724.
- [31] F. Yu, J. Zhan, D. Chen, J. Guo, S. Zhang, L.H. Zhang, Electronic states regulation induced by the synergistic effect of Cu clusters and Cu-S₁N₃ sites boosting electrocatalytic performance, Adv. Funct. Mater. 33 (2023) 2214425.
- [32] Z. Lin, Y. Wang, Z. Peng, Y.C. Huang, F. Meng, J.L. Chen, C.L. Dong, Q. Zhang, R. Wang, D. Zhao, Single-metal atoms and ultra-small clusters manipulating charge carrier migration in polymeric perylene diimide for efficient photocatalytic oxygen production, Adv. Energy Mater. 12 (2022) 2200716.
- [33] Z. Liu, S. Yao, A. Zhang, Y. Li, Y. Fu, Q. Zhou, Intramolecular built-in electric field enhanced polymerized nitrogen-carbon homojunction π*-electron delocalization enrichment promotes photocatalytic uranium (VI) reduction, Appl. Catal. B: Environ. (2023) 123023.
- [34] Y. Qin, J. Lu, F. Meng, X. Lin, Y. Feng, Y. Yan, M. Meng, Rationally constructing of a novel 2D/2D WO₃/Pt/g-C₃N₄ Schottky-Ohmic junction towards efficient visible-light-driven photocatalytic hydrogen evolution and mechanism insight, J. Colloid Interface Sci. 586 (2021) 576–587.
- [35] M. Wang, G. Tan, S. Feng, M. Dang, Y. Wang, B. Zhang, H. Ren, L. Lv, A. Xia, W. Liu, Y. Liu, Defects and internal electric fields synergistically optimized g-C₃N₄_x/BiOCl/WO_{2.92} heterojunction for photocatalytic NO deep oxidation, J. Hazard Mater. 408 (2021) 124897.
- [36] R. Tang, D. Gong, Y. Deng, S. Xiong, J. Zheng, L. Li, Z. Zhou, L. Su, J. Zhao, pi-pi stacking derived from graphene-like biochar/g-C₃N₄ with tunable band structure for photocatalytic antibiotics degradation via peroxymonosulfate activation, J. Hazard Mater. 423 (2022) 126944.
- [37] L. Sun, B. Li, X. Chu, N. Sun, Y. Qu, X. Zhang, I. Khan, L. Bai, L. Jing, Synthesis of Si-O-Bridged g-C₃N₄/WO₃ 2D-heterojunctional nanocomposites as efficient photocatalysts for aerobic alcohol oxidation and mechanism insight, ACS Sustain. Chem. Eng. 7 (2019) 9916–9927.
- [38] W. Wang, S. Song, P. Wang, M. He, Z. Fang, X. Yuan, H. Li, C. Li, X. Wang, Y. Wei, Chemical Bonding of g-C₃N₄/UiO-66 (Zr/Ce) from Zr and Ce Single Atoms for Efficient Photocatalytic Reduction of CO₂ under Visible Light, ACS Catal. 13 (2023) 4597–4610.
- [39] F. Xing, C. Wang, S. Liu, S. Jin, H. Jin, J. Li, Interfacial chemical bond engineering in a direct Z-Scheme g-C₃N₄/MoS₂ heterojunction, ACS Appl. Mater. Interfaces 15 (2023) 11731–11740.
- [40] H. Ren, F. Qi, A. Labidi, J. Zhao, H. Wang, Y. Xin, J. Luo, C. Wang, Chemically bonded carbon quantum dots/Bi₂WO₆ S-scheme heterojunction for boosted photocatalytic antibiotic degradation: Interfacial engineering and mechanism insight, Appl. Catal. B: Environ. 330 (2023) 122587.

- [41] B. Li, S. Liu, C. Lai, G. Zeng, M. Zhang, M. Zhou, D. Huang, L. Qin, X. Liu, Z. Li, N. An, F. Xu, H. Yi, Y. Zhang, L. Chen, Unravelling the interfacial charge migration pathway at atomic level in 2D/2D interfacial Schottky heterojunction for visible-light-driven molecular oxygen activation, *Appl. Catal. B Environ.* 266 (2020) 118650.
- [42] Z. Liu, H. Xiang, A. Zhang, L. Wu, Y. Fu, Q. Zhou, Enhancing photocatalytic antibiotics mineralization and water oxidation via constructing interfacial electric field in plate-on-plate BiOCl/WO₃ photocatalysts, *J. Colloid Interface Sci.* 642 (2023) 264–272.
- [43] K. Gao, M. Zhou, Y. Liu, S. Wang, R. Fu, Z. Wang, J. Guo, Z. Liu, H. Wang, Y. Zhao, Q. Wang, The dual built-in electric fields across CoS/MoS₂ heterojunctions for energy-saving hydrogen production coupled with sulfion degradation, *J. Colloid Interface Sci.* 657 (2024) 290–299.
- [44] L. Pan, M. Ai, C. Huang, L. Yin, X. Liu, R. Zhang, S. Wang, Z. Jiang, X. Zhang, J.-J. Zou, W. Mi, Manipulating spin polarization of titanium dioxide for efficient photocatalysis, *Nat. Commun.* 11 (2020) 418.
- [45] X. Shen, W. Liu, X. Gao, Z. Lu, X. Wu, X. Gao, Mechanisms of oxidase and superoxide dismutation-like activities of gold, silver, platinum, and palladium, and their alloys: a general way to the activation of molecular oxygen, *J. Am. Chem. Soc.* 137 (2015) 15882–15891.
- [46] Y. Shi, Z. Yang, L. Shi, H. Li, X. Liu, X. Zhang, J. Cheng, C. Liang, S. Cao, F. Guo, X. Liu, Z. Ai, L. Zhang, Surface boronizing can weaken the excitonic effects of biobr nanosheets for efficient O₂ activation and selective NO oxidation under visible light irradiation, *Environ. Sci. Technol.* 56 (2022) 14478–14486.
- [47] Q. Wang, D. Xu, Y. Dong, S. Pang, L. Zhang, G. Zhang, L. Lv, X. Liu, Y. Xia, L. C. Campos, Z. Ren, P. Wang, Unsaturated Nd-Bi dual-metal sites enable efficient NIR light-driven O₂ activation for water purification, *Appl. Catal. B Environ.* 319 (2022) 121924.
- [48] S. Zhang, C. Tan, R. Yan, X. Zou, F.L. Hu, Y. Mi, C. Yan, S. Zhao, Constructing built-in electric field in heterogeneous nanowire arrays for efficient overall water electrolysis, *Angew. Chem.* 135 (2023) e202302795.
- [49] M.-Y. Gao, C.-C. Li, H.-L. Tang, X.-J. Sun, H. Dong, F.-M. Zhang, Boosting visible-light-driven hydrogen evolution of covalent organic frameworks through compositing with MoS₂: a promising candidate for noble-metal-free photocatalysts, *J. Mater. Chem. A* 7 (2019) 20193–20200.